Palaeogeography, Palaeoclimatology, Palaeoecology 634 (2024) 111927

Contents lists available at ScienceDirect

Palaeogeography, Palaeoclimatology, Palaeoecology

journal homepage: www.elsevier.com/locate/palaeo

Intensive chemical weathering in the Arctic during the Miocene Climatic Optimum

Adrian M. Hall [a,*], Dan N. Barfod [b], H. Albert Gilg [c,*], Finlay M. Stuart [d], Pertti Sarala [e], Thair Al-Ani [f]

[a] Institute of Geography, University of Edinburgh, Drummond Street, Edinburgh EH8 9XP, UK
[b] NEIF Argon Isotope Laboratory, Scottish Universities Environmental Research Centre, Scottish Enterprise Park, East Kilbride G75 0QF, UK
[c] Engineering Geology, TUM School of Engineering and Design, Technical University of Munich, Arcisstr. 21, 80333 Munich, Germany
[d] Scottish Universities Environmental Research Centre, Scottish Enterprise Park, East Kilbride G75 0QF, UK
[e] Oulu Mining School, University of Oulu, FI-90014, Finland
[f] Geological Survey of Finland (GTK), Vuorimiehentie 5, 02151 Espoo, Finland

ARTICLE INFO

Editor: H Falcon-Lang

Keywords:
Miocene Climatic Optimum
Weathering
Arctic
Cryptomelane, climate change

ABSTRACT

The Arctic today has shallow, chemically immature, and frost-dominated weathering regimes. At Sokli, Finland (68°N), a 70 m deep palaeo-weathering profile is developed in a Devonian carbonatite pipe that represents fundamentally different past weathering environments. Formation of the apatite-francolite P-ore likely began under Palaeogene warm, humid climates. Later, cryptomelane (K-Mn oxide) crusts developed within the ore that have yielded peak $^{40}Ar/^{39}Ar$ ages of 16.20 ± 0.13 Ma (2σ)., The crusts formed at the redox front during the Miocene Climatic Optimum (~16.9–14.7 Ma) under mean annual temperatures ~12–14 °C warmer than today. The presence of the cryptomelane crust at shallow depth (15 m) indicates very low erosion rates since formation, consistent with its position on a tectonically stable Archaean craton and in the cold-based ice-divide zone of successive Fennoscandian ice sheets. The Miocene Climatic Optimum triggered a pulse of intensive weathering in mid- and low latitudes; the Sokli cryptomelane ages demonstrate that intensive chemical weathering extended into the Arctic.

1. Introduction

During the Cenozoic, the Earth's climate changed from the "hot-house" of the Palaeocene-Eocene to be eventually replaced by the "ice-house" of the Pleistocene. In the fluctuating climates of the last 25 My, the warmest period was the Miocene Climatic Optimum (MCO), a global greenhouse interval with pCO_2 (~400–600 ppm) that provides an analogue for future climate scenarios (Steinthorsdottir et al., 2021b). MCO warming was associated with a phase of intensive weathering at mid-latitudes (Brlek et al., 2021; Wan et al., 2009), but the responses of Arctic weathering systems remains largely unknown despite their importance for geochemical fluxes (Beaulieu et al., 2012) and in modulating climate change though drawdown of atmospheric carbon (De Vleeschouwer et al., 2020). This knowledge gap exists partly because few Paleogene and Neogene weathering profiles survived erosion by Pleistocene ice sheets. Two rare examples of intensive weathering inside the Arctic Circle occur at Sokli, northern Finland, and at neighbouring Kovdor on the Kola Peninsula, Russia (Fig. 1) where Devonian carbonatite intrusions are weathered to depths of many tens of metres (Broom-Fendley et al., 2021). The weathering is distinct in depth, fines concentration, and advanced geochemical alteration from Holocene skeletal soils (Darmody et al., 2008), Middle Pleistocene interglacial palaeosols (Olsson and Melkerud, 2000) and Neogene to early Pleistocene sandy saprolites (Hall et al., 2015) found elsewhere in northernmost Fennoscandia. Here we provide the first absolute age determinations for this palaeo-weathering. $^{40}Ar/^{39}Ar$ dating of cryptomelane, a K-Mn oxide, indicates formation of late-stage weathering crusts at Sokli during the MCO and shows that intensive weathering extended into the Arctic at this time.

2. Regional setting

The Sokli complex in eastern Finnish Lapland (67°48′ N, 29°27′ E) occupies a circular topographic basin ~5 km in diameter and is

* Corresponding author.
E-mail address: adrian.hall@ed.ac.uk (A.M. Hall).

https://doi.org/10.1016/j.palaeo.2023.111927
Received 14 September 2023; Received in revised form 16 November 2023; Accepted 16 November 2023
Available online 22 November 2023
0031-0182/© 2023 The Authors. Published by Elsevier B.V. This is an open access article under the CC BY license (http://creativecommons.org/licenses/by/4.0/).

surrounded by low hills reaching up to ~320 m a.s.l. Sokli is the westernmost member of the Kola Alkaline Province (Fig. 1), intruded into Archean Belomorian group rocks at about 360 Ma (Kramm et al., 1993). The Archean country rocks are foliated tonalitic migmatites and mafic to ultramafic volcanic rocks. The intrusive complex (Fig. 2) is composed of a core, 6.4 km in diameter, of phoscorite, calcite, and dolomite carbonatites, with outer rings of carbonatite and fenite, that are crosscut by late Sr-, REE- and Ba-bearing veins (Lee et al., 2003; Lee et al., 2006; Vartiainen, 1980; Vartiainen and Paarma, 1979). Sokli has been a target for mineral exploration in Finland due to its large P reserves and Nb, Ta and REEs hosted in accessory minerals (Al-Ani and Sarapää, 2013a, 2016).

Sokli lies on the backslope of the Barents Sea passive margin (Fig. 1). On the foreslope in the Kola peninsula, average exhumation since 1.9 Ga is estimated at ~1–2 m/Myr from thermochronology (Veselovskiy et al., 2019). Average post-Devonian exhumation at 3 m/Myr is estimated from the erosion depth of the carbonatite pipe at Sokli (Hall, 2015). The preservation of the small (1.5 km diameter) Saarijärvi impact crater in northern Finland (Fig. 1) which retains Ediacaran and Early Cambrian claystones (Öhman, 2007) is also consistent with slow Phanerozoic erosion at Sokli and Kola and with low exhumation rates on the craton further south (Hall et al., 2021).

Uplift along the Barents Sea passive margin in the Late Cretaceous-Palaeocene (Hendriks and Andriessen, 2002; Redfield and Osmundsen, 2013) led to erosion in northern Norway and Sweden and development of stepped erosion surfaces (Ebert et al., 2011; Lidmar-Bergström et al., 2007; Schermer et al., 2017). Palaeogene marine diatoms are reworked into Pleistocene deposits in Finnish Lapland that overlie or lie close to deep weathering localities. The marine diatoms have been interpreted as a record of Eocene marine transgression of the basement (Tynni, 1982), implying a pre-Eocene age for the underlying weathering (Söderman, 1985). However, an alternative hypothesis regards the diatoms as reworked by winds blowing across exposed Eocene sediments on the Barents Sea shelf during the Pleistocene (Hall and Ebert, 2013). Other sedimentary evidence of Eocene marine transgression is lacking.

Late Cenozoic global cooling brought the Arctic into the periglacial zone after ~3.0 Ma, with extensive development of ground ice (Wennrich et al., 2016). Advancing ice sheets generally acted to remove weathering covers developed earlier in the Cenozoic at high and mid-latitudes (Clark and Pollard, 1998). Sokli, however, lay beneath the ice-divide zone of the Fennoscandian ice sheet during the Pleistocene (Hirvas, 1991). Cold-based conditions at the ice sheet bed allowed widespread preservation of Neogene landforms and deep weathering covers (Hall et al., 2015). Cosmogenic nuclide evidence suggests exposure and survival of fragile granite tors through multiple glacial cycles over the last 0.65–1.0 Ma (Darmody et al., 2008; Stroeven et al., 2002). Limited glacial erosion at Sokli is indicated by clasts derived from the alkaline igneous complex and its weathering mantle which occur in local tills and esker gravels (Perttunen and Vartiainen, 1992). The basin floor holds a detailed, near-continuous, sedimentary sequence for the last interglacial-glacial cycle (Helmens et al., 2015).

The carbonatite weathering at Sokli has been described as a Fe-P-Nb-laterite and comprises loose, wet, and ferruginous earthy and stony regolith, which is light to dark brown in colour due to fine-grained goethite, and nearly black in its manganese-rich parts (Pehkonen-Ollila and Gehör, 2007) (Fig. 3A, B). Weathering depths are generally 5–30 m below glacial deposits (Vartiainen and Paarma, 1979), reaching 107 m (Broom-Fendley et al., 2021) (Fig. 3C). Three generations of francolite, a secondary carbonate fluorapatite form of phosphate, are recognised at Sokli (Vartiainen and Paarma, 1979). The P-ore developed after complex weathering, leaching, recrystallization, and lithification (O'Brien and Hyvonen, 2015). Intense weathering led to (i) enrichment of apatite following dissolution of carbonates, (ii) formation of francolite, (iii) local replacement of phlogopite by vermiculite (Rama et al., 2020), (iv) intense alteration of olivine, (v) the partial replacement of magnetite by hematite, (vi) alteration of pyrochlore, and (vii) the total removal of sulphides (O'Brien and Hyvonen, 2015). The aureole rocks are mainly decomposed to hydromica-apatite, with an intensely weathered soft, dark green-brown, upper layer and a partly weathered, lower blocky regolith. At Kovdor, 50 km ESE of Sokli, carbonatites are brecciated (Krasnova et al., 2004; Lapin and Lyagushkin, 2014) and host francolites reach depths of 70–100 m (Broom-Fendley et al., 2021). At least four generations of apatite–francolite ore genesis have been identified (Lapin and Lyagushkin, 2014). At Seblyavr, weathering is generally thin but crater-like depressions in the weathering front are reported to reach depths of 220 m (Nivin et al., 2003), although the contribution of metasomatism to alteration is unclear (Kalashnikov et al., 2016).

At Sokli, existing P-ore is locally enriched in Fe-Mn oxides, including

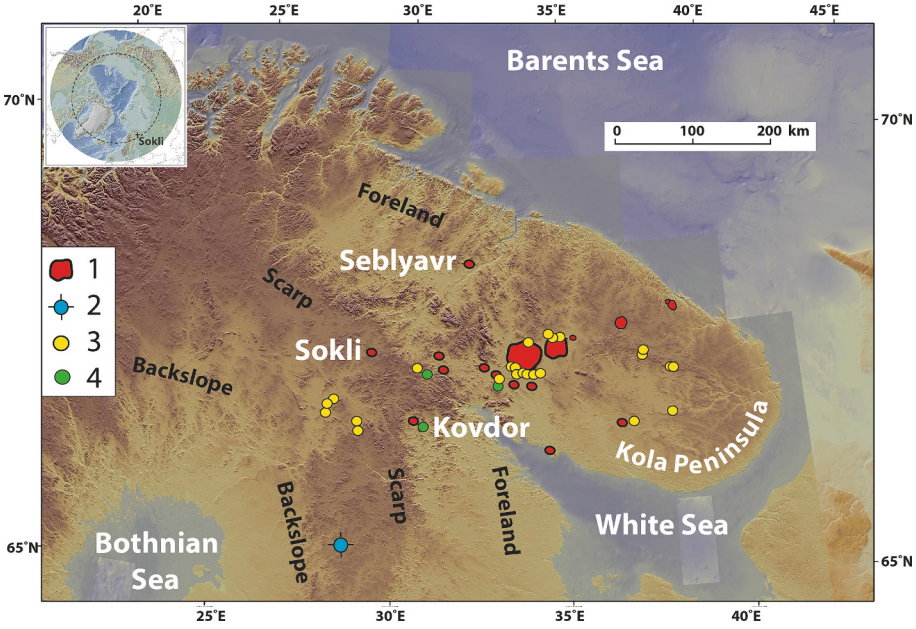

Fig. 1. The Barents Sea passive margin, with the locations of the weathered carbonatites at Sokli, Kovdor, and Seblyavr. 1. Intrusions of the Devonian Kola Alkaline Intrusive Province. 2. Impact structure at Saarijärvi. 3. Kaolinite weathering localities. 4. Sungulite weathering localities.

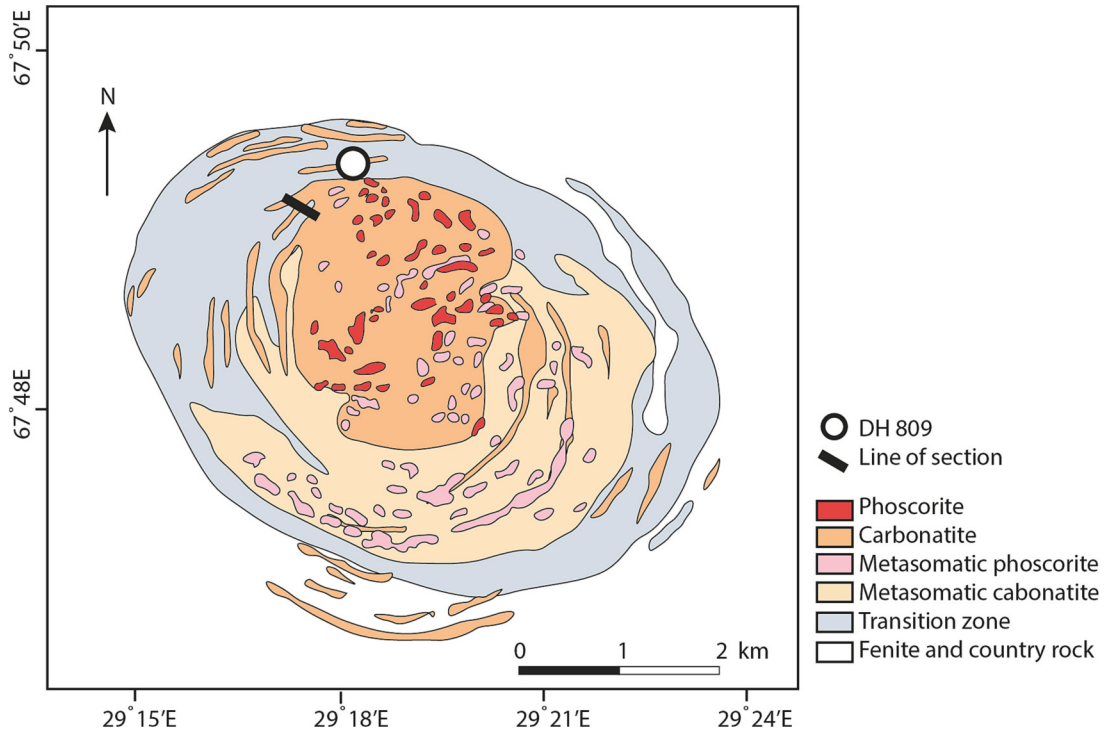

Fig. 2. The geology of the Sokli carbonatite intrusion and its aureole (modified from Al-Ani et al., 2018). Sample borehole DH 809 and the line of section WR 58 to 47 are shown.

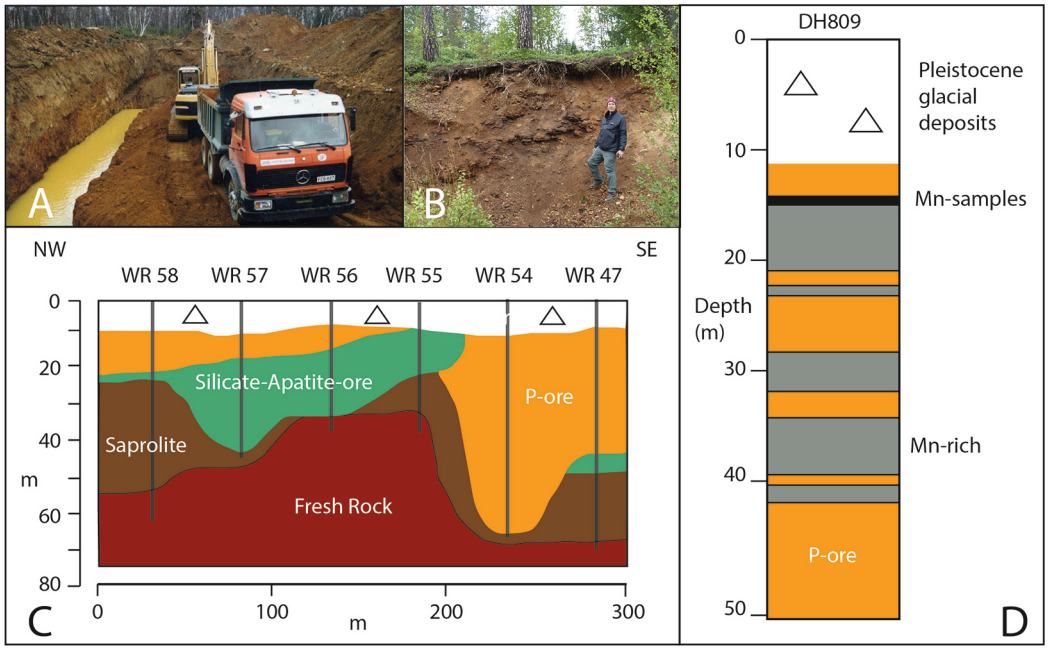

Fig. 3. Weathered carbonatite at Sokli. A. Excavation in lateritic P-ore. Image courtesy of Yara Mining. B. Surface exposure in ore with diffuse Mn-oxides. C. Weathering profile in carbonatite at Vainio, Sokli, modified from Pehkonen-Ollila and Gehör (2007)Pehkonen-Ollila and Gehör (2007). Line of section from boreholes WR 58 to 47 is shown in Figure 1. D. Summary log of drill core DH809. Courtesy of the Finnish Minerals Group.

cryptomelane, a black K-(Ba-Sr-Pb)-bearing Mn-oxide. Dense, pure Mn oxide orecretes form close to the redox front under conditions of permanent or seasonal moisture saturation (Dill et al., 2010). At Sokli, these conditions developed beneath the floor of the enclosing topographic basin. Cryptomelane has been used widely in dating weathering phases (Vasconcelos and Carmo, 2018) and provides a first opportunity to date the late weathering phases at Sokli.

3. Samples and methods

The carbonatite weathering profiles are currently exposed at Sokli in partially vegetated test trenches and mine cuts (Fig. 3). Secondary K-Mn oxides are present locally in thin layers close to the ground surface (Pehkonen-Ollila and Gehör, 2007) and at depths of up to 40 m (Al-Ani and Sarapää, 2013b).

Mineralogical analyses: We collected hard, black Mn-oxide rich samples at depths of 13.65–16.65 m from borehole DH809 in francolite ore (Fig. 3D). The drill core sample (6 cm diameter) was cut into the 4 slices (A to D; Fig. 4A) each about 7 mm thick; three of them A,B, and D, were investigated. The cryptomelane samples were very hard and required crushing using a steel piston, and were then sieved to isolate the 100–400 μm size fraction, washed with water, and dried in an oven at 40 °C. The size fractions were handpicked under binocular microscope to remove obvious apatite-containing grains and vugs. Aliquots of the three 100–400 μm fractions and of the three handpicked mineral separates from the 100–400 μm fractions were ground in an agate mortar, mounted on a single crystal silicon plate with acetone. The air-dried random powder mounts were analysed by X-ray diffraction (XRD) using a Bruker D8 Advance Eco (Bragg-Brentano geometry, Cu anode, 40 kV, 25 mA, automatic divergence slit, 15 mm irradiated sample length, motorized anti-air-scatter, 2.5° primary and secondary sollers, 2–70° 2 Theta, 0.01° step size, 1 s/step). Samples were mounted for examination under a Scanning Electron Microscope (SEM: Hitachi SU 5000 Schottky) equipped with energy-dispersive X-ray emission (EDX) spectrometry (AztecEnergy). All mineralogical analyses were carried out at TUM School of Engineering and Design and Department of Earth and Environmental Sciences, Ludwig-Maximilians University, Munich.

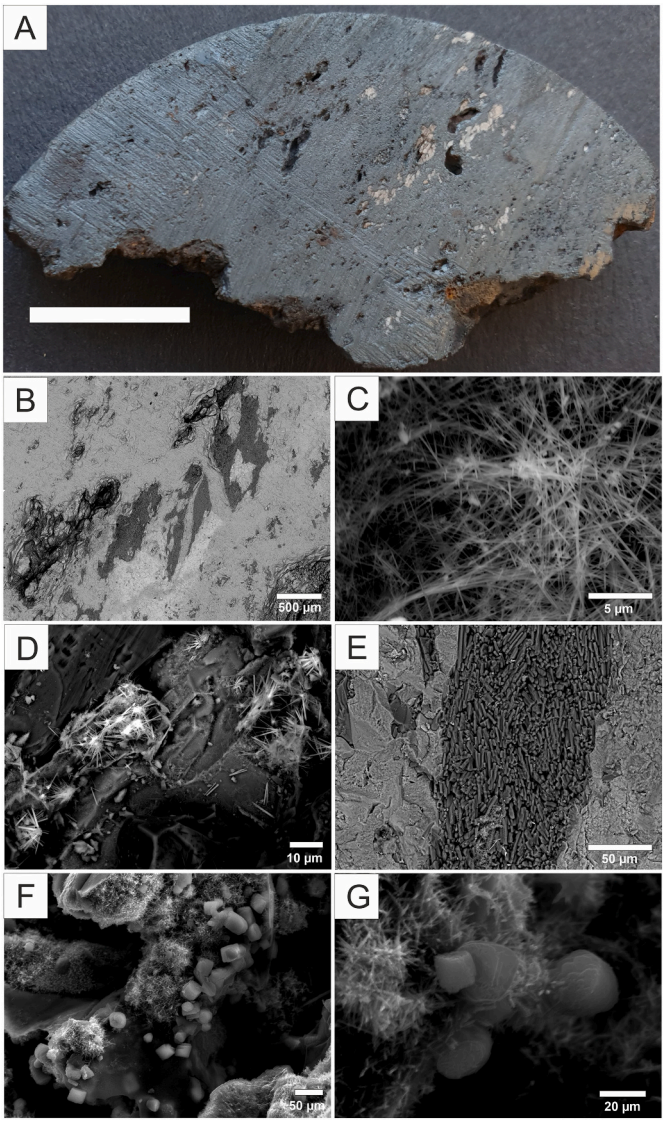

Fig. 4. Cryptomelane and associated minerals at Sokli. A. Photograph of sample SO-09D showing grey dense to locally porous secondary indurated manganese oxide and the residual white and brown apatite-rich inclusions (scale bar = 1 cm). B. Secondary electron (SE) image of a cut sample from the block shown in Figure 4A under the scanning electron microscope (SEM). Dark grey areas of apatite are visible and light grey cryptomelane, plus some voids. The slightly brighter areas in cryptomelane have more Ba and Sr than the darker ones. C. Detail of hair-like cryptomelane in the vugs. D. Bright cryptomelane needles on apatite. E. More massive cryptomelane forms (light grey) and etched apatite (dark grey). F. Small cubes of crandallite group minerals (mostly REE-Ca-Sr-Ba-aluminium phosphates). G. Crandallite cubes growing on cryptomelane needles.

Argon isotope dating: Bulk samples were hand crushed and sieved to an approximately 1.0 mm diameter grain size. Using a binocular picking microscope, grains that were visibly free of alteration or mineral inclusions were selected for analysis (Vasconcelos et al., 1994). Samples and neutron flux monitors were packaged within wells in machined aluminium discs and stacked in quartz tubes with the relative positions of wells precisely measured for later reconstruction of neutron flux gradients. The sample package was irradiated in the Oregon State University reactor, Cd-shielded facility. Fish Canyon sanidine standard (28.294 ± 0.036, 1σ) Ma (Renne et al., 2011) was used to monitor ^{39}Ar production and establish neutron flux values (J parameter, see Table S1) for the samples. Gas was extracted from samples via step-heating using a mid-infrared (10.6 μm) CO_2 laser with a non-gaussian, uniform energy profile and a 3.5 mm beam diameter centred over a sample well. The samples were loaded into a copper planchette containing 56 circular wells of 4 mm diameter and housed in a doubly pumped ZnS-window laser cell. All argon isotope analyses were carried out at the NEIF Argon Isotope Laboratory.

Each aliquot consisted of 3–4 fragments (~4–6 mg) that were step-heated together. Due to the low degassing temperatures of cryptomelane, the duration of each heating step was reduced to a 2 s ramp followed by 1 s at the specified power for a total of 3 s of lasing. The flux of joules delivered to the sample well is specified in the data table (Table S1) for each step.

Liberated argon was purified in two stages. The first stage of cleaning (originally designed for alunite analyses) exposed liberated gases to ~0.5 g of silver wire bundles, polished copper (of the planchette), a charcoal cryotrap held at 200 K to trap water, and a hot Zr-Al getter at 400 °C. Second stage cleaning involved further gettering with two Zr-Al getters; one at 16 °C and another at 400 °C.

Data were collected on a Mass Analyser Products MAP-215-50 single-collector mass spectrometer using an electron multiplier collector in dynamic collection (peak hopping) mode. Time-intensity data are regressed to inlet time with second-order polynomial fits to the data. Mass discrimination was monitored between and within sample runs by analysis of an air standard aliquot delivered by an automated pipette. All blank, interference and mass discrimination corrections and age calculations were performed with the MassSpec software package (MassSpec, version 8.058, authored by Al Deino, Berkeley Geochronology Center). Decay constants (Table S1) are listed in Renne et al., 2011.

4. Results

X-ray diffraction analysis of bulk powders showed that sample material contains >90% cryptomelane, a black K-(Ba-Sr-Pb)-bearing Mn-oxide (ideal endmember KMn_8O_{16}) with minor fluorapatite (Fig. S4). In the handpicked fractions, no phases other than cryptomelane were detected by XRD analysis. SEM-EDX analysis of cryptomelane shows predominant K, but also some Ba- and Sr-enriched areas are visible (Fig. 4B). The whitish and brownish spots in the dark grey Mn-oxide are residual apatite (Fig. 4A). Strongly etched surfaces are seen under SEM (Fig. 4E). The cryptomelane forms needle-like crystals with an aspect ratio of 20 to 60 that are extremely thin (diameter < 1 μm) in open vugs (Fig. 4C), but much thicker (>1 μm) in the massive part (Fig. 4D). Cryptomelane forms a dense mass elsewhere (Fig. 4E). Small cubes of crandallite group minerals (Ba-, Sr-, Pb-, and REE-bearing aluminium

phosphates) are crystallized in vugs on the fine cryptomelane needles close to residual apatite (Fig. 4F,G).

Three samples of cryptomelane (SO-9A, 9C, 9D) were analysed by $^{40}Ar/^{39}Ar$ step-heating in triplicate (De Putter and Ruffet, 2020; Li and Vasconcelos, 2002; Vasconcelos et al., 1994) for a total of nine age determinations (Fig. 5). Isochrons, using only the plateau steps, for all experiments yielded ages concordant with their respective plateau ages. The isochron plots also indicate that all trapped component intercepts are indistinguishable from air and that no resolvable excess ^{40}Ar is apparent in the experiments (Fig. 6). See the Appendix for analytical details (Table S1) and data plots (Figs. S1-S3). Two samples (SO-9C and SO-9D) yielded indistinguishable plateau ages for all three aliquots within a given sample (Figs. S1 and S2). Five of the age spectra plots from samples 9A(2), 9C(2), 9D(1,2,3,) show initial steps with lower ages, typically several Ma younger than the later plateau steps (Figs. S1-S3). Sample SO-9A gave two analyses (1 & 2) with younger plateau ages and a third plateau age similar to the ages given by the -9C and -9D samples (Fig. S3).

The reproducibility of ages between different aliquots of a given sample led us to combine these into composite plateau ages for SO-9C and 9D and for two of the experiments from SO-9A, yielding more precise results for these samples of 15.78 ± 0.21, 16.49 ± 0.18 and 13.07 ± 0.51 Ma (Table S1). Composite plateau ages were determined by combining all accepted plateau steps from the individual aliquots and calculating an inverse-variance weighted mean age. These results imply resolvable gaps between these ages of 0.7 ± 0 0.4 and 2.7 ± 0.7 Myr, and a gap of 3.4 ± 0.7 Myr from the highest to lowest values.

Sample SO-9A records two distinct ages, 13.07 ± 0.51 Ma (composite plateau age of aliquots 1 & 2) and 16.08 ± 0.48 Ma, indicating spatial age heterogeneity within the sample. Analysed fragments of the samples were approximately 1 mm in diameter and derived from a single larger fragment of a few cm diameter. This would suggest cm-scale or finer spatio-temporal heterogeneity within the sample, similar to that reported in other cryptomelane studies (Li et al., 2007; Vasconcelos and Conroy, 2003).

All step heating experiments are presented as age probability plots (Figs. S1-S3). One hundred and forty four individual steps were analysed. Steps with low gas yields (<0.1 mV ^{39}Ar, approximate blank level), or imprecise analyses (age uncertainty >60%) are excluded, removing 53 steps. The impact of excluding these points is low, typically <0.1% of the peak ages.

The remaining individual steps from all nine experiments ($n = 91$) were combined into an age probability plot (Fig. 5) that has a bimodal distribution. The data were filtered against MSWD criteria to extract two coherent gaussian populations, rejecting 7 steps as too high or low relative to the peak ages. The seven rejected steps occur at either the beginning or end of the step heating spectra, account for <5% of released ^{39}Ar in a given step and typically have large uncertainties and/or are very air-rich implying large atmospheric corrections. The rejection has a minimal impact on the interpretation of the remainder of the data.

The age-probability plot reveals a strong clustering of step ages at 16.20 ± 0.13 Ma (2σ, $n = 57$). This age overlaps with or is close to the older plateau ages from the step heating experiments and their respective composite ages. Notably, the two younger experiments from SO-9A (1 & 2), with a composite plateau age of 13.07 ± 0.51 Ma are significantly younger and overlap with the lower probability younger peak at ca. 12.89 ± 0.43 Ma (2σ, $n = 27$) on the age probability plot.

The data show age reproducibility within samples and similarities between samples. These features have been recognised in similar studies employing cryptomelane $^{40}Ar/^{39}Ar$ dating and have been taken as strong evidence for interpreting the ages as recording weathering events. (Feng and Vasconcelos, 2001; Vasconcelos and Conroy, 2003). We interpret our data as representing a main phase of cryptomelane formation at ca. 16.2 Ma as evidenced by the probability density function peak age. The interpretation of the probability density function as a proxy for volume or rate of formation is sensitive to assumptions about representative sampling. That is, the age data yield only temporal information and thus can only give a qualitative picture of changes in the formation rates of the system. If representative of crystallisation rate, the decreasing number of younger step ages suggests that the process of cryptomelane formation, though active, was waning after 16.2 Ma. Younger step ages in some of the samples that yielded plateaus, e.g., of samples SO-9C (2) and 9D (1,2,3), may reflect this later formation. In

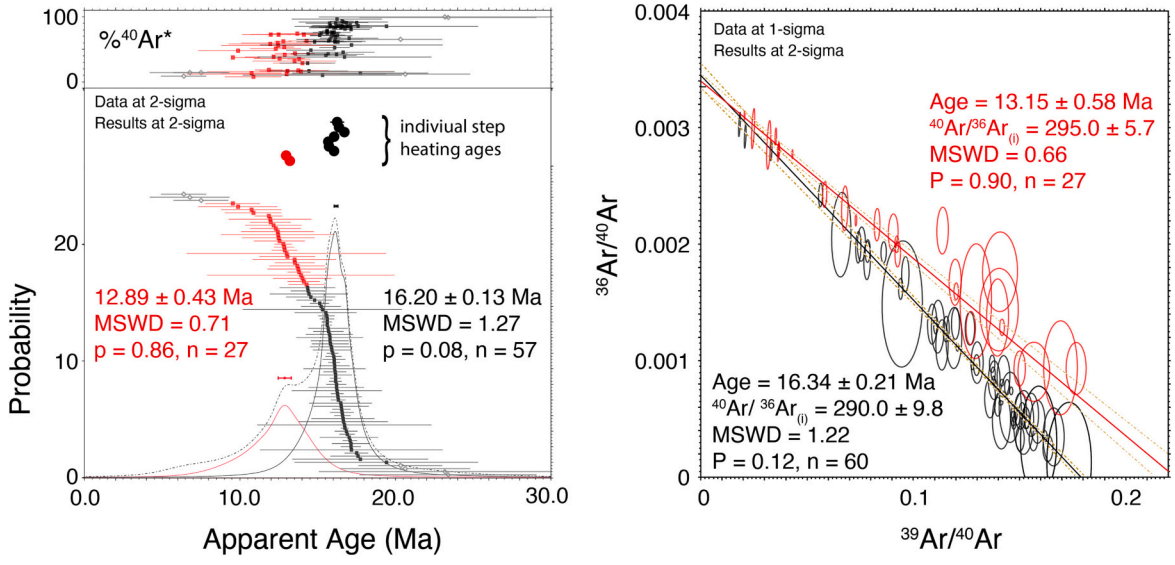

Fig. 5. Age probability and isochron plot of $^{40}Ar/^{39}Ar$ data for all steps, from all step-heating experiments (9 aliquots). Left-hand panel shows age probability plot of 91 individual steps out of 144 individual analyses; 53 steps were discarded due to low gas yields (<0.1 mV ^{39}Ar) or high age uncertainties (>60%). Subsets of 57 (black) and 27 (red) steps that form coherent populations yield ages of 16.20 ± 0.13 Ma for the main peak age and 12.89 ± 0.43 Ma for the younger, smaller peak. Gray symbols are excluded by the data filtering. Plateau ages for individual experiments are shown for comparison ("individual step heating ages" -larger circle symbols with error bars), showing agreement with the age probability plot peaks. Upper portion of the plot shows that the selected analyses have significant radiogenic argon, with the majority of data >30% $^{40}Ar^*$. The right-hand panel shows the isochrons for the selected steps yielding ages that are indistinguishable from the age probability peaks and trapped components indistinguishable from air (298.56 ± 0.31).

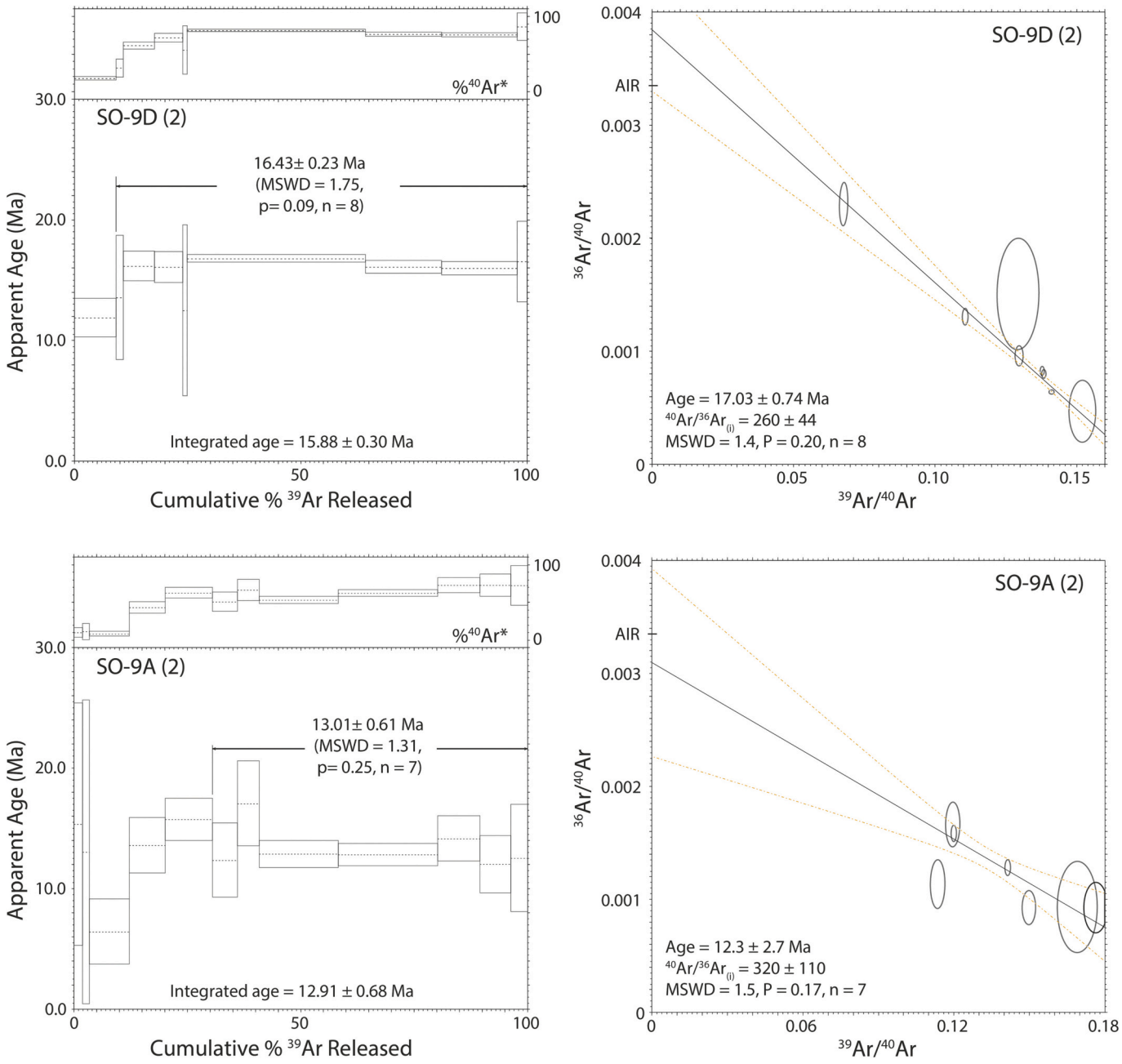

Fig. 6. Example plateau diagrams and associated isochrons for SO-9D (2) and SO-9A (2). Plateau diagrams show data at 2s uncertainty and results at 2s uncertainty, excluding J error. Isochron diagrams show data at 1s and results at 2s, also excluding J error. The plateau for 9D gives an age of 16.43 ± 0.23 Ma with satisfactory statistical criterion (MSWD<2) and the requisite gas yield and number of steps (91% ^{39}Ar and n=8). The isochron, composed of the plateau steps, yields an age indistinguishable from the plateau age and a trapped ^{40}Ar/^{36}Ar component indistinguishable from air (298.56 ± 0.31). The plateau shows an early, younger step at ca. 13 Ma, typical of many of the experiments from this sample suite. Sample SO-9A (2) yields a younger plateau age of 13.01 ± 0.62 Ma with a younger early step, and a concordant isochron with an atmospheric trapped component.

this case, the gaps between the plateau ages of SO-9C and 9D and the much later ages from SO-9A may reflect multiple events of formation or subsequent events of recrystallisation over a 3.4 ± 0.7 Myr period, from approximately 16.5 to 13.1 Ma. Both the peak formation age (16.2 Ma) and the inferred more protracted age range are coincident with the timing and duration of the MCO. Greater textural information and spatial extent of sampling coupled with better analytical precision would be needed to clarify any temporal variations in the rate of formation.

Younger ages from the age probability plot and younger plateau ages at ca. 13 Ma may attest to protracted formation, later recrystallisation or recoil redistribution (Ren and Vasconcelos, 2019; Vasconcelos et al., 1994) in the cryptomelane.

Recoil redistribution, that is, ejection of ^{39}Ar and subsequent reimplantation, is a potential explanation for two younger aliquots of sample 9A (1 & 2) as both of the step heating releases show disturbance with rising and then falling ages in the initial steps, although this is most clearly seen in aliquot 9A (2) and further recoil interpretation is limited by the resolution of the data (Fig. S3). We note though that the plateaus defined for these samples are composed of the later steps in the release whereas apparent disturbance is generally found in the early steps, suggesting that recoil is an unlikely explanation for the young plateaus. Furthermore, we believe that a recoil mechanism would not generate a well-defined peak in the age probability plot and we therefore suggest

that protracted formation or later recrystallisation are the preferred interpretations (Vasconcelos et al., 1995). We suggest that 16.2 ± 0.13 Ma is the most robust and secure estimate of when cryptomelane was forming at Sokli.

5. Discussion and conclusions

The texture and paragenetic minerals of apatite-francolite ores at Sokli and Kovdor resemble deeply weathered carbonatites developed under humid tropical climates (Broom-Fendley et al., 2021; De Toledo et al., 2004). These include carbonatite palaeo-weathering profiles, including those of Permian age on the North Siberian Plain (70–73°N) (Lapin et al., 2016) (Fig. 7) and Cretaceous age in Ontario, Canada (50°N) (Sage, 1991). Overlying Fe- and Mn-rich horizons have been largely removed by erosion at Sokli, as on the nearby carbonatite pipe at Kovdor (Lapin and Lyagushkin, 2014). Only the roots of the supergene profiles remain (Lapin and Lyagushkin, 2014).

The initiation and duration of weathering for the thick carbonatite weathering profiles remain poorly constrained. Multiple phases of francolite formation at Sokli and Kovdor indicate complex, and potentially long weathering histories. Thick weathering mantles on Kola have been interpreted as Mesozoic in age (Afanas'ev Afanas'ev, 1977). Remoteness from post-Devonian sedimentary cover and deep erosion in response to Late Cretaceous-Palaeocene uplift along the Barents Sea margin (Hendriks and Andriessen, 2002) make exhumation of paleo-weathering of similar age unlikely at Sokli. Geochemical evidence indicates enhanced weathering around the Arctic Ocean around the Palaeocene-Eocene Thermal Maximum (Dickson et al., 2015; Wieczorek et al., 2013). Weathering profiles of 20–40 m thickness are developed on Precambrian gneisses in northern Finland (Gilg et al., 2013; Lintinen and Al-Ani, 2005) and on Kola (Evzerov et al., 2007) and include saprolites rich in kaolinite and "sungulite", a lizardite-bearing pseudomorph after vermiculite (Kiselev, 1979) (Fig. 1). D/H and $^{18}O/^{16}O$ ratios indicate kaolin formation in northern Finland under mean annual temperatures of 13–15 °C; these temperatures last prevailed in this part of the Arctic during the Palaeogene or Miocene (Gilg et al., 2013). Hence, deep weathering profiles in Devonian carbonatite and Archaean gneisses may overlap in age. The cryptomelane at Sokli was precipitated during the Miocene within an existing porous and openwork regolith (Vartiainen and Paarma, 1979) and provides a minimum age for earlier phase(s) of carbonatite weathering. The preservation of cryptomelane at shallow depth (14–17 m) at Sokli requires very low average erosion rates since formation, consistent with its cratonic setting (Veselovskiy et al., 2019) and position beneath the cold-based ice-divide zone of the Pleistocene Fennoscandian ice sheet (Putkinen et al., 2020). A detailed record of long-term weathering and denudation clearly exists on the Barents Sea passive margin, but further absolute age determinations of the P-ores at Sokli, Kovdor, and Seblyavr, and for kaolins and "sungulites" found more widely across northern Fennoscandia (Fig. 1) are necessary to unlock the full weathering history.

The existing carbonatite weathering profile at Sokli was reactivated over a period of at least 3.4 ± 0.7 My, with the main phase of

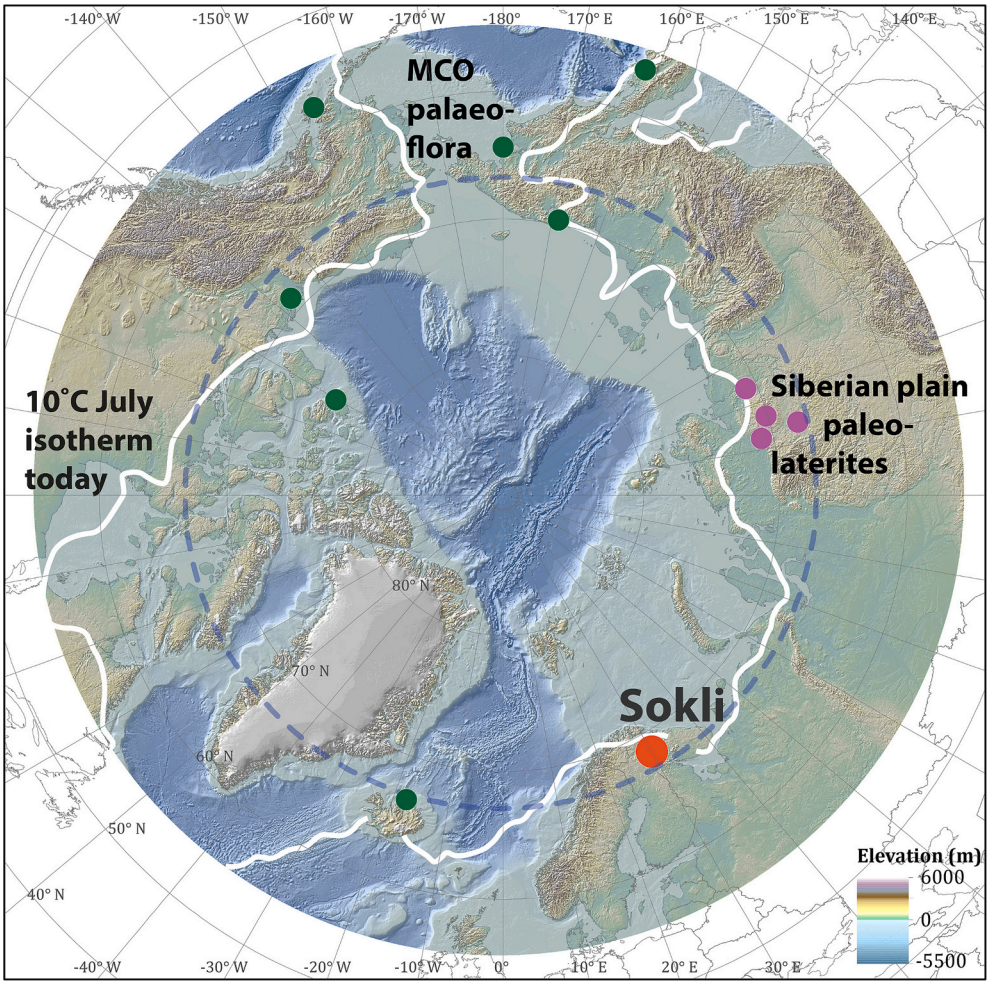

Fig. 7. Arctic location of Sokli, with locations for paleo-laterites (Lapin et al., 2016) and key sites for MCO palaeofloras (Denk et al., 2011; Popova et al., 2012; White et al., 1997). Digital Elevation Model from the GEBCO_2014 Grid, version 20,150,318, http://www.gebco.net. (For interpretation of the references to colour in this figure legend, the reader is referred to the web version of this article.)

cryptomelane precipitation occurring during the Miocene Climatic Optimum (~16.9–14.7 Ma). The MCO is a part of the Monterey carbon isotope excursion (MCIE)—a prolonged ~1.0 ‰ positive carbon isotope excursion ($\delta^{13}C$) of the global oceans (Sosdian et al., 2020). The MCO was characterized by a substantial high latitude warming of ~8 K, indicating a weak meridional temperature gradient compared to today (Tanner et al., 2020). In the Arctic, humid temperate climates prevailed, with cool mixed deciduous forests at 70–74°N and an absence of summer sea-ice (Pound et al., 2012; Steinthorsdottir et al., 2021a). Palaeo-floral assemblages around the Arctic (Fig. 7) indicate moist Middle Miocene conditions. MATs reached 11–13 °C in lowland Iceland (Denk et al., 2011), ≥ 13.6 °C in western Siberia (Popova et al., 2012). and 11.5 °C at Cook Inlet, Alaska (White et al., 1997). Modern MATs are ~1 °C at Sokli; MCO MATs were likely ~12–14 °C warmer. The present-day 10 °C July isotherm lies close to Sokli today (Fig. 7) but lay towards the pole during the MCO, leaving the Arctic Ocean largely or wholly free of sea ice in model scenarios (Lohmann et al., 2022).

Further south in Europe, temperature and precipitation increased during the MCO (Bruch et al., 2011) and led to a spike in weathering intensity. Deep weathering profiles of middle Miocene age are widespread (Migoń and Lidmar-Bergström, 2002), with lateritic bauxite development in central and eastern Europe (Böhme, 2003; Brlek et al., 2021; Schwarz, 1997). Cryptomelane crusts developed during the MCO in southern Germany (Dill and Wemmer, 2012) and towards the base of kaolinitic deep weathering profiles in the Ardennes (Demoulin et al., 2018) but other K-Mn crust ages in the Vosges and Schwarzwald massifs span the Miocene without apparent concentration at the MCO (Hautmann and Lippolt, 2000). Soil temperatures exceeded 30 °C in the Alpine foreland basin (Methner et al., 2020). In the western USA (45°N), lateritic bauxites developed on Columbia River Basalts from 15.7 Ma (Liu et al., 2013). Intensified weathering during the MCO is also recognised at mid-latitudes in the Southern Hemisphere (Vasconcelos et al., 2013; Vasconcelos et al., 2015) and at low latitudes (Jean et al., 2020; Wan et al., 2009). Sokli provides the first evidence that intensive weathering extended into the Arctic during the MCO.

Weathering in the Arctic today is dominated by frost processes and chemical weathering is suppressed by low temperatures, limited availability of liquid water, low vegetation productivity, and low rainfall. Yet the Arctic is warming rapidly (Overland et al., 2019), with recent warming of surface air temperatures around the Barents Sea of 2.7C per decade (Isaksen et al., 2022), bringing major consequences for regional and global climate, ecosystems, and human activity (Landrum and Holland, 2020). The Arctic weathering system is strongly sensitive to future climate change due to the availability of fresh, comminuted rock and mineral debris (Beaulieu et al., 2012; Millot et al., 2002; Tank et al., 2012) and the potential for rapid soil formation in a greening Arctic (Doetterl et al., 2022). Present day atmospheric CO_2 concentrations of 419 ppm approach or exceed most estimated ranges for CO_2 concentrations in the MCO of 300–500 ppm (Greenop et al., 2014), ~470–630 ppm (Sosdian et al., 2020) and 450–550 ppm (Steinthorsdottir et al., 2021b)]. The present trajectory of climate change is towards a return of the warmth that last prevailed in the MCO (Steinthorsdottir et al., 2021a). The evidence from Sokli for intensive weathering during the MCO suggests that future Arctic warming may lead to a fundamental reset in its weathering systems.

Declaration of Competing Interest

The authors declare that they have no known competing financial interests or personal relationships that could have appeared to influence the work reported in this paper.

Data availability

Data will be made available on request.

Acknowledgements

The work described in this paper was supported by the Albert & Maria Bergström's Foundation and the NERC funded NEIF Argon Isotope Laboratory. AMH is grateful for logistical support from Seppo Gehör at Yara Suomi Oy and Teo Lehto at Sokli Oy. We thank Paolo Vasconcelos and one anonymous reviewer for constructive criticism.

Appendix A. Supplementary data

Supplementary data to this article can be found online at https://doi.org/10.1016/j.palaeo.2023.111927.

References

Afanas'ev, A.P., 1977. Phanerozoic Weathering Crusts of the Baltic Shield and Related Mineral Resources (in Russian). Nauka, Leningrad.
Al-Ani, T., Molnár, F., Lintinen, P., Leinonen, S., 2018. Geology and Mineralogy of Rare Earth Elements Deposits and Occurrences in Finland. Minerals 8, 356.
Al-Ani, T., Sarapää, O., 2013a. Geochemistry and mineral phases of REE in Jammi carbonatite veins and fenites, southern end of the Sokli complex, NE Finland. In: Geochemistry: Exploration, Environment, Analysis, 13, pp. 217–224.
Al-Ani, T., Sarapää, O., 2013b. Mineralogical and geochemical study on carbonatites and fenites from the Kaulus drill cores, southern side of the Sokli complex, NE Finland. Geol. Surv. Finland Arch. Rep. 145, 66.
Al-Ani, T., Sarapää, O., 2016. Abundance of REE-Bearing Minerals in Carbonatite and Lamprohyre Dikes in Kaulus Area, Sokli Carbonatite Complex, NE Finland. Geological Survey of Finland, p. 27.
Beaulieu, E., Goddéris, Y., Donnadieu, Y., Labat, D., Roelandt, C., 2012. High sensitivity of the continental-weathering carbon dioxide sink to future climate change. Nat. Clim. Chang. 2, 346–349.
Böhme, M., 2003. The Miocene climatic optimum: evidence from ectothermic vertebrates of Central Europe. Palaeogeogr. Palaeoclimatol. Palaeoecol. 195, 389–401.
Brlek, M., Gaynor, S.P., Mongelli, G., Bauluz, B., Sinisi, R., Brčić, V., Peytcheva, I., Mišur, I., Tapster, S., Trinajstić, N., Laita, E., Yuste, A., Šuica, S., Grizelj, A., Kukoč, D., Schaltegger, U., 2021. Karst bauxite formation during Miocene Climatic Optimum (Central Dalmatia, Croatia): mineralogical, compositional and geochronological perspectives. Int. J. Earth Sci. 110, 2899–2922.
Broom-Fendley, S., Siegfried, P.R., Wall, F., O'Neill, M., Brooker, R.A., Fallon, E.K., Pickles, J.R., Banks, D.A., 2021. The origin and composition of carbonatite-derived carbonate-bearing fluorapatite deposits. Mineral. Deposita 56, 863–884.
Bruch, A.A., Utescher, T., Mosbrugger, V., 2011. Precipitation patterns in the Miocene of Central Europe and the development of continentality. Palaeogeogr. Palaeoclimatol. Palaeoecol. 304, 202–211.
Clark, P.U., Pollard, D., 1998. Origin of the middle Pleistocene transition by ice sheet erosion of regolith. Palaeoceanography 13, 1–9.
Darmody, R.G., Thorn, C.E., Seppala, M., Campbell, S.W., Li, Y.K., Harbor, J., 2008. Age and weathering status of granite tors in Arctic Finland (~ 68° N). Geomorphology 94, 10–23.
De Putter, T., Ruffet, G., 2020. Supergene manganese ore records 75 Myr-long Campanian to Pleistocene geodynamic evolution and weathering history of the Central African Great Lakes Region – Tectonics drives, climate assists. Gondwana Res. 83, 96–117.
De Toledo, M.C.M., Lenharo, S.L., Ferrari, V.C., Fontan, F., De Parseval, P., Leroy, G., 2004. The compositional evolution of apatite in the weathering profile of the Catalão I alkaline-carbonatitic complex, Goiás, Brazil. Can. Mineral. 42, 1139–1158.
De Vleeschouwer, D., Drury, A.J., Vahlenkamp, M., Rochholz, F., Liebrand, D., Pälike, H., 2020. High-latitude biomes and rock weathering mediate climate–carbon cycle feedbacks on eccentricity timescales. Nat. Commun. 11, 5013.
Demoulin, A., Barbier, F., Dekoninck, A., Verhaert, M., Ruffet, G., Dupuis, C., Yans, J., 2018. Erosion surfaces in the Ardenne–Oesling and their associated kaolinic weathering mantle. In: Landscapes and Landforms of Belgium and Luxembourg. Springer, pp. 63–84.
Denk, T., Grímsson, F., Zetter, R., Símonarson, L.A., 2011. The Archaic Floras, Late Cainozoic Floras of Iceland: 15 Million Years of Vegetation and Climate History in the Northern North Atlantic. Springer, Netherlands, Dordrecht, pp. 173–231.
Dickson, A.J., Cohen, A.S., Coe, A.L., Davies, M., Shcherbinina, E.A., Gavrilov, Y.O., 2015. Evidence for weathering and volcanism during the PETM from Arctic Ocean and Peri-Tethys osmium isotope records. Palaeogeogr. Palaeoclimatol. Palaeoecol. 438, 300–307.
Dill, H.G., Wemmer, K., 2012. Origin and K/Ar age of cryptomelane-bearing Sn placers on silcretes, SE Germany. Sediment. Geol. 275-276, 70–78.
Dill, H.G., Hansen, B., Keck, E., Weber, B., 2010. Cryptomelane: A tool to determine the age and the physical–chemical regime of a Plio-Pleistocene weathering zone in a granitic terrain (Hagendorf, SE Germany). Geomorphology 121, 370–377.
Doetterl, S., Alexander, J., Fior, S., Frossard, A., Magnabosco, C., van de Broek, M., Westergaard, K.B., 2022. Will accelerated soil development be a driver of Arctic Greening in the late 21st century? J. Plant Nutr. Soil Sci. 185, 19–23.
Ebert, K., Hättestrand, C., Hall, A.M., Alm, G., 2011. DEM identification of macro-scale stepped relief in arctic northern Sweden. Geomorphology 132, 339–350.

Evzerov, V., Pripachkin, P., Dudkin, K., 2007. Linear weathering crust of the Fedorova-Pana layered complex in the northeastern Baltic Shield. Dokl. Earth Sci. 413, 170–172.
Feng, Y., Vasconcelos, P., 2001. Quaternary continental weathering geochronology by laser-heating $^{40}Ar/^{39}Ar$ analysis of supergene cryptomelane. Geology 29, 635–638.
Gilg, H.A., Hall, A.M., Ebert, K., Fallick, A.E., 2013. Cool kaolins in Finland. Palaeogeogr. Palaeoclimatol. Palaeoecol. 392, 454–462.
Greenop, R., Foster, G.L., Wilson, P.A., Lear, C.H., 2014. Middle Miocene climate instability associated with high-amplitude CO2 variability. Paleoceanography 29, 845–853.
Hall, A.M., 2015. Phanerozoic denudation across the Kola Peninsula, northwest Russia: implications for long term stability of Precambrian shield margins. Nor. J. Geol. 95, 27–43.
Hall, A.M., Ebert, K., 2013. Cenozoic microfossils in northern Finland: local reworking or distant wind transport? Palaeogeogr. Palaeoclimatol. Palaeoecol. 388, 1–14.
Hall, A.M., Sarala, P., Ebert, K., 2015. Late Cenozoic deep weathering patterns on the Fennoscandian shield in northern Finland: a window on ice sheet bed conditions at the onset of Northern Hemisphere glaciation. Geomorphology 246, 472–488.
Hall, A.M., Putkinen, N., Hietala, S., Lindsberg, E., Holma, M., 2021. Ultra-slow cratonic denudation in Finland since 1.5 Ga indicated by tiered unconformities and impact structures. Precambrian Res. 352, 106000.
Hautmann, S., Lippolt, H., 2000. $^{40}Ar/^{39}Ar$ dating of central European K–Mn oxides—a chronological framework of supergene alteration processes during the Neogene. Chem. Geol. 170, 37–80.
Helmens, K.F., Salonen, J.S., Plikk, A., Engels, S., Väliranta, M., Kylander, M., Brendryen, J., Renssen, H., 2015. Major cooling intersecting peak Eemian Interglacial warmth in northern Europe. Quat. Sci. Rev. 122, 293–299.
Hendriks, B.W., Andriessen, P.A., 2002. Pattern and timing of the post-Caledonian denudation of northern Scandinavia constrained by apatite fission-track thermochronology. Geol. Soc. Lond. Spec. Publ. 196, 117–137.
Hirvas, H., 1991. Pleistocene stratigraphy of Finnish Lapland. Geol. Surv. Finland Bull. 354, 1–123.
Isaksen, K., Nordli, Ø., Ivanov, B., Køltzow, M.A.Ø., Aaboe, S., Gjelten, H.M., Mezghani, A., Eastwood, S., Førland, E., Benestad, R.E., Hanssen-Bauer, I., Brækkan, R., Sviashchennikov, P., Demin, V., Revina, A., Karandasheva, T., 2022. Exceptional warming over the Barents area. Sci. Rep. 12, 9371.
Jean, A., Beauvais, A., Chardon, D., Arnaud, N., Jayananda, M., Mathe, P., 2020. Weathering history and landscape evolution of Western Ghats (India) from $^{40}Ar/^{39}Ar$ dating of supergene K–Mn oxides. J. Geol. Soc. Lond. 177, 523–536.
Kalashnikov, A., Konopleva, N., Pakhomovsky, Y.A., Ivanyuk, G.Y., 2016. Rare earth deposits of the Murmansk region, Russia—a review. Econ. Geol. 111, 1529–1559.
Kiselev, I.I., 1979. The palaeogeography of the western Kola peninsula during the Neogene and Antropogene (in Russian). Izvestiya Vsesoyuznogo Geograficheskogo Obshchestva 111, 316–324.
Kramm, U., Kogarko, L., Kononova, V., Vartiainen, H., 1993. The Kola Alkaline Province of the CIS and Finland: Precise Rb-Sr ages define 380–360 Ma age range for all magmatism. Lithos 30, 33–44.
Krasnova, N., Balaganskaya, E., Garcia, D., 2004. Kovdor—classic phoscorites and carbonatites. In: Wall, F., A.N., Z. (Eds.), Phoscorites and Carbonatites from Mantle to Mine: The Key Example of the Kola Alkaline Province. Mineralogical Society, London, pp. 95–127.
Landrum, L., Holland, M.M., 2020. Extremes become routine in an emerging new Arctic. Nat. Clim. Chang. 10, 1108–1115.
Lapin, A., Lyagushkin, A., 2014. The Kovdor apatite-francolite deposit as a prospective source of phosphate ore. Geol. Ore Deposits 56, 61–80.
Lapin, A.V., Tolstov, A.V., Kulikova, I.M., 2016. Distribution of REE, Y, Sc, and Th in the unique complex rare-metal ores of the Tomtor deposit. Geochem. Int. 54, 1061–1078.
Lee, M.J., Garcia, D., Moutte, J., Lee, J.I., 2003. Phlogopite and tetraferriphlogopite from phoscorite and carbonatite associations in the Sokli massif, Northern Finland. Geosci. J. 7, 9–20.
Lee, M.J., Lee, J.I., Garcia, D., Moutte, J., Williams, C.T., Wall, F., Kim, Y., 2006. Pyrochlore chemistry from the Sokli phoscorite-carbonatite complex, Finland: Implications for the genesis of phoscorite and carbonatite association. Geochem. J. 40, 1–13.
Li, J.-W., Vasconcelos, P., 2002. Cenozoic continental weathering and its implications for the palaeoclimate: evidence from $^{40}Ar/^{39}Ar$ geochronology of supergene K–Mn oxides in Mt Tabor, central Queensland, Australia. Earth Planet. Sci. Lett. 200, 223–239.
Li, J.-W., Vasconcelos, P., Zhang, W., Deng, X.-D., Duzgoren-Aydin, N., Yan, D.-R., Zhang, J.-Q., Hu, M.-A., 2007. Timing and duration of supergene mineralization at the Xinrong manganese deposit, western Guangdong Province, South China: cryptomelane $^{40}Ar/^{39}Ar$ dating. Mineral. Deposita 42, 361–383.
Lidmar-Bergström, K., Näslund, J.-O., Ebert, K., Neubeck, T., Bonow, J., 2007. Cenozoic landscape development on the passive margin of northern Scandinavia. Nor. J. Geol. 87, 181–196.
Lintinen, P., Al-Ani, T., 2005. The Vittajänkä kaolin deposit, Salla, Finnish Lapland. Geol. Surv. Finland Spec. Pap. 38, 41–47.
Liu, X.-M., Rudnick, R.L., McDonough, W.F., Cummings, M.L., 2013. Influence of chemical weathering on the composition of the continental crust: Insights from Li and Nd isotopes in bauxite profiles developed on Columbia River Basalts. Geochim. Cosmochim. Acta 115, 73–91.
Lohmann, G., Knorr, G., Hossain, A., Stepanek, C., 2022. Effects of CO_2 and ocean mixing on miocene and pliocene temperature gradients. Paleoceanogr. Paleoclimatol. 37 e2020PA003953.
Methner, K., Campani, M., Fiebig, J., Löffler, N., Kempf, O., Mulch, A., 2020. Middle Miocene long-term continental temperature change in and out of pace with marine climate records. Sci. Rep. 10, 7989.
Migoń, P., Lidmar-Bergström, K., 2002. Deep weathering through time in central and northwestern Europe: problems of dating and interpretation of geological record. Catena 49, 25–40.
Millot, R., Gaillardet, J., Dupré, B., Allègre, C.J., 2002. The global control of silicate weathering rates and the coupling with physical erosion: new insights from rivers of the Canadian Shield. Earth Planet. Sci. Lett. 196, 83–98.
Nivin, V., Liferovich, R., Ikorsky, S., Balaganskaya, E., Subbotin, V., 2003. Noble gas isotopes in minerals from phoscorites and carbonatites in Kovdor and Seblyavr ultramafic-alkaline complexes (Kola alkaline province, NW Russia). Period. Mineral. 72, 135–145.
O'Brien, E.H., Hyvonen, E., 2015. The Sokli carbonatite complex. In: Maier, W., O'Brien, H., Lahtinen, R. (Eds.), Mineral Deposits of Finland. Elsevier, Amsterdam, pp. 305–326.
Öhman, T., 2007. The Origin and Tectonic Modification of the Saarijärvi Impact Structure, Northern Finland, Workshop on Impact Cratering II. Saint-Hubert, Canada, Lunar and Planetary Institute, Houston, Texas, pp. 85–86.
Olsson, M.T., Melkerud, P.A., 2000. Weathering in three podzolized pedons on glacial deposits in northern Sweden and Central Finland. Geoderma 94, 149–161.
Overland, J., Dunlea, E., Box, J.E., Corell, R., Forsius, M., Kattsov, V., Olsen, M.S., Pawlak, J., Reiersen, L.-O., Wang, M., 2019. The urgency of Arctic change. Polar Sci. 21, 6–13.
Pehkonen-Ollila, A.-R., Gehör, S., 2007. Mineral Chemistry of Pyrochlore in Residually Inherited Fe-P-Nb-Laterite Ore Bodies at Sokli Carbonatite Complex, Goldschmidt Conference Abstracts 2007. Cologne, Germany, p. A771.
Perttunen, M., Vartiainen, H., 1992. Glaciofluvial transport of clasts and heavy minerals from the Sokli carbonatite complex, Finnish Lapland. Geol. Surv. Finland Bull. 366, 21.
Popova, S., Utescher, T., Gromyko, D., Bruch, A., Mosbrugger, V., 2012. Palaeoclimate evolution in Siberia and the Russian Far East from the Oligocene to Pliocene–evidence from fruit and seed floras. Turk. J. Earth Sci. 21, 315–334.
Pound, M.J., Haywood, A.M., Salzmann, U., Riding, J.B., 2012. Global vegetation dynamics and latitudinal temperature gradients during the Mid to late Miocene (15.97–5.33 Ma). Earth Sci. Rev. 112, 1–22.
Putkinen, N., Sarala, P., Eyles, N., Daxberger, H., Pihlaja, J., Murray, A., 2020. Reworked Middle Pleistocene deposits preserved in the core region of the Fennoscandian Ice Sheet. Quat. Sci. Adv. 2, 100005.
Rama, M., Eklund, O., Fröjdö, S., Smått, J.-H., Lastusaari, M., Laiho, T., 2020. Characterization of altered mica from Sokli, Northern Finland. Clay Clay Miner. 1–11.
Redfield, T., Osmundsen, P., 2013. The long-term topographic response of a continent adjacent to a hyperextended margin: A case study from Scandinavia. Geol. Soc. Am. Bull. 125, 184–200.
Ren, Z., Vasconcelos, P.M., 2019. Quantifying ^{39}Ar recoil in natural hypogene and supergene alunites and jarosites. Geochim. Cosmochim. Acta 260, 84–98.
Renne, P.R., Balco, G., Ludwig, K.R., Mundil, R., Min, K., 2011. Response to the comment by WH Schwarz et al. on "Joint determination of 40K decay constants and $^{40}Ar^*/^{40}K$ for the fish Canyon sanidine standard, and improved accuracy for $^{40}Ar/^{39}Ar$ geochronology" by PR Renne et al.(2010). Geochim. Cosmochim. Acta 75, 5097–5100.
Sage, R.P., 1991. Geology of the Martison Carbonatite Complex; Ontario, Open File Report. Geological Survey of Canada, pp. 1–74.
Schermer, E.R., Redfield, T.F., Indrevær, K., Bergh, S.G., 2017. Geomorphology and topography of relict surfaces: the influence of inherited crustal structure in the northern Scandinavian Mountains. J. Geol. Soc. Lond. 174, 93–109.
Schwarz, T., 1997. Lateritic bauxite in Central Germany and implications for Miocene palaeoclimate. Palaeogeogr. Palaeoclimatol. Palaeoecol. 129, 37–50.
Söderman, G., 1985. Planation and weathering in eastern Fennoscandia. Fennia 163, 347–352.
Sosdian, S., Babila, T., Greenop, R., Foster, G., Lear, C., 2020. Ocean carbon storage across the middle Miocene: A new interpretation for the Monterey Event. Nat. Commun. 11, 1–11.
Steinthorsdottir, M., Coxall, H.K., de Boer, A.M., Huber, M., Barbolini, N., Bradshaw, C. D., Burls, N.J., Feakins, S.J., Gasson, E., Henderiks, J., Holbourn, A.E., Kiel, S., Kohn, M.J., Knorr, G., Kürschner, W.M., Lear, C.H., Liebrand, D., Lunt, D.J., Mörs, T., Pearson, P.N., Pound, M.J., Stoll, H., Strömberg, C.A.E., 2021a. The Miocene: the future of the past. Paleoceanogr. Paleoclimatol. 36 e2020PA004037.
Steinthorsdottir, M., Jardine, P.E., Rember, W.C., 2021b. Near-future pCO_2 during the Hot Miocene Climatic Optimum. Paleoceanogr. Paleoclimatol. 36 e2020PA003900.
Stroeven, A.P., Fabel, D., Hättestrand, C., Harbor, J., 2002. A relict landscape in the Centre of Fennoscandian glaciation: cosmogenic radionuclide evidence of tors preserved through multiple glacial cycles. Geomorphology 44, 145–154.
Tank, S.E., Raymond, P.A., Striegl, R.G., McClelland, J.W., Holmes, R.M., Fiske, G.J., Peterson, B.J., 2012. A land-to-ocean perspective on the magnitude, source and implication of DIC flux from major Arctic rivers to the Arctic Ocean. Glob. Biogeochem. Cycles 26.
Tanner, T., Hernández-Almeida, I., Drury, A.J., Guitián, J., Stoll, H., 2020. Decreasing atmospheric CO_2 during the late Miocene Cooling. Paleoceanogr. Paleoclimatol. 35 e2020PA003925.
Tynni, R., 1982. The reflection of geological evolution in Tertiary and interglacial diatoms and silicoflagellates in Finnish Lapland. Geol. Surv. Finland Bull. 320, 1–64.
Vartiainen, H., 1980. The petrography, mineralogy and petrochemistry of the Sokli carbonatite massif, northern Finland. Geol. Surv. Finland Bull. 313, 1–126.

Vartiainen, H., Paarma, H., 1979. Geological characteristics of the Sokli carbonatite complex, Finland. Econ. Geol. 74, 1296–1306.
Vasconcelos, P.M., Carmo, I.D.O., 2018. Calibrating denudation chronology through $^{40}Ar/^{39}Ar$ weathering geochronology. Earth Sci. Rev. 179, 411–435.
Vasconcelos, P.M., Conroy, M., 2003. Geochronology of weathering and landscape evolution, Dugald River valley, NW Queensland, Australia. Geochim. Cosmochim. Acta 67, 2913–2930.
Vasconcelos, P.M., Brimhall, G.H., Becker, T.A., Renne, P.R., 1994. $^{40}Ar/^{39}Ar$ analysis of supergene jarosite and alunite: Implications to the paleoweathering history of the western USA and West Africa. Geochim. Cosmochim. Acta 58, 401–420.
Vasconcelos, P.M., Renne, P.R., Becker, T.A., Wenk, H.-R., 1995. Mechanisms and kinetics of atmospheric, radiogenic, and nucleogenic argon release from cryptomelane during 40Ar39Ar analysis. Geochim. Cosmochim. Acta 59, 2057–2070.
Vasconcelos, P.M., Heim, J.A., Farley, K.A., Monteiro, H., Waltenberg, K., 2013. $^{40}Ar/^{39}Ar$ and (U–Th)/He–$^{4}He/^{3}He$ geochronology of landscape evolution and channel iron deposit genesis at Lynn Peak, Western Australia. Geochim. Cosmochim. Acta 117, 283–312.
Vasconcelos, P.M., Reich, M., Shuster, D.L., 2015. The paleoclimatic signatures of supergene metal deposits. Elements 11, 317–322.
Veselovskiy, R.V., Thomson, S.N., Arzamastsev, A.A., Botsyun, S., Travin, A.V., Yudin, D. S., Samsonov, A.V., Stepanova, A.V., 2019. Thermochronology and Exhumation history of the Northeastern Fennoscandian Shield since 1.9 Ga: evidence from $^{40}Ar/^{39}Ar$ and Apatite Fission Track Data from the Kola Peninsula. Tectonics 38, 2317–2337.
Wan, S., Kürschner, W.M., Clift, P.D., Li, A., Li, T., 2009. Extreme weathering/erosion during the Miocene Climatic Optimum: evidence from sediment record in the South China Sea. Geophys. Res. Lett. 36.
Wennrich, V., Andreev, A.A., Tarasov, P.E., Fedorov, G., Zhao, W., Gebhardt, C.A., Meyer-Jacob, C., Snyder, J.A., Nowaczyk, N.R., Schwamborn, G., Chapligin, B., Anderson, P.M., Lozhkin, A.V., Minyuk, P.S., Koeberl, C., Melles, M., 2016. Impact processes, permafrost dynamics, and climate and environmental variability in the terrestrial Arctic as inferred from the unique 3.6 Myr record of Lake El'gygytgyn, Far East Russia – A review. Quat. Sci. Rev. 147, 221–244.
White, J., Ager, T., Adam, D., Leopold, E., Liu, G., Jette, H., Schweger, C., 1997. An 18 million year record of vegetation and climate change in northwestern Canada and Alaska: tectonic and global climatic correlates. Palaeogeogr. Palaeoclimatol. Palaeoecol. 130, 293–306.
Wieczorek, R., Fantle, M.S., Kump, L.R., Ravizza, G., 2013. Geochemical evidence for volcanic activity prior to and enhanced terrestrial weathering during the Paleocene Eocene thermal Maximum. Geochim. Cosmochim. Acta 119, 391–410.